



## Article

# High-Performance Asymmetric Optical Transmission Based on a Dielectric–Metal Metasurface

Wenbing Liu , Lirong Huang \*, Jifei Ding, Chenkai Xie, Yi Luo and Wei Hong \*

Wuhan National Laboratory for Optoelectronics, Huazhong University of Science and Technology, 1037 Luoyu Rd, Wuhan 430074, China; D201780662@hust.edu.cn (W.L.); D201880718@hust.edu.cn (J.D.); M201972863@hust.edu.cn (C.X.); D202080923@hust.edu.cn (Y.L.)

\* Correspondence: lrhuang@mail.hust.edu.cn (L.H.); w.hong@hust.edu.cn (W.H.)

**Abstract:** Asymmetric optical transmission plays a key role in many optical systems. In this work, we propose and numerically demonstrate a dielectric–metal metasurface that can achieve high-performance asymmetric transmission for linearly polarized light in the near-infrared region. Most notably, it supports a forward transmittance peak (with a transmittance of 0.70) and a backward transmittance dip (with a transmittance of 0.07) at the same wavelength of 922 nm, which significantly enhances operation bandwidth and the contrast ratio between forward and backward transmittances. Mechanism analyses reveal that the forward transmittance peak is caused by the unidirectional excitation of surface plasmon polaritons and the first Kerker condition, whereas the backward transmittance dip is due to reflection from the metal film and a strong toroidal dipole response. Our work provides an alternative and simple way to obtain high-performance asymmetric transmission devices.

**Keywords:** metasurface; asymmetric optical transmission; surface plasmon polaritons; Kerker conditions



**Citation:** Liu, W.; Huang, L.; Ding, J.; Xie, C.; Luo, Y.; Hong, W.

High-Performance Asymmetric Optical Transmission Based on a Dielectric–Metal Metasurface.

*Nanomaterials* **2021**, *11*, 2410.

<https://doi.org/10.3390/nano11092410>

Academic Editors:

Andrey B. Evlyukhin  
and Jose A. Sanchez-Gil

Received: 22 August 2021

Accepted: 14 September 2021

Published: 16 September 2021

**Publisher's Note:** MDPI stays neutral with regard to jurisdictional claims in published maps and institutional affiliations.



**Copyright:** © 2021 by the authors. Licensee MDPI, Basel, Switzerland. This article is an open access article distributed under the terms and conditions of the Creative Commons Attribution (CC BY) license (<https://creativecommons.org/licenses/by/4.0/>).

## 1. Introduction

Asymmetric optical transmission refers to different transmittance responses when a beam of light passes through a medium in forward and backward directions. Over the past few decades, due to its indispensable role in many optical systems, asymmetric transmission (AT) has attracted great attention in various applications, such as optical isolating [1,2], optical diodes [3,4], noise control or cancelation [5,6], systems for one-side detection/sensing [7,8], etc. One conventional way to achieve AT devices is to take advantage of non-reciprocity, which can be obtained by using magneto-optical materials [9,10] or nonlinear effects [11]. However, it is difficult to achieve on-chip integration due to their bulky size and the requirement of high threshold operating intensity.

Fortunately, the emergence of metamaterial provides an appealing alternative to control electromagnetic wave manipulations properties [12–17], and the discovery of the AT phenomenon based on metamaterial was first experimentally demonstrated in the microwave region by Fedotov et al. in 2006 [18]. Since then, various AT devices based on artificial structures have been proposed which use photonic crystals [19,20], subwavelength asymmetric gratings [21–24], chiral metamaterials [25–27] and metasurfaces [28–30], and the operation wavelengths have been covered from microwave to visible light [31–33]. These devices show promise to some degree; however, those using chiral metamaterials are usually complex and incorporate multilayer structures, whereas those using subwavelength asymmetric gratings are polarization sensitive. Therefore, it is still highly desirable to develop polarization-insensitive AT devices with simpler structures, polarization independence and higher contrast ratios between forward and backward transmittances.

Here, we employ a dielectric–metal metasurface to realize high-performance asymmetric transmission (AT) for linearly polarized light at the near-infrared region. Its structural unit consists of a dielectric ( $\text{Al}_2\text{O}_3$ ) disk and a thin layer of gold (Au) film on a  $\text{SiO}_2$  substrate. Simulation results show that it supports a forward transmittance peak (with a

transmittance of 0.70) and a backward transmittance dip (with a transmittance of 0.07) at 922 nm. The occurrence of a forward transmission peak and backward transmission dip at the same wavelength notably enhances operation bandwidth and the contrast ratio between the forward and backward transmittances. This is quite different from previously reported works: to the knowledge of the authors, such a phenomenon has not been reported yet. Here, it is revealed that unidirectional surface plasmon polaritons (SPPs) excitation and Kerker conditions are responsible for the emergence of the forward transmittance peak, while the reflection from the metal layer and strong toroidal dipole response are responsible for the backward transmittance dip.

The rest of the paper is organized as follows: In Section 2, we present the device structure and operation principle. In Section 3, we first interpret the origin of the AT effect by using unidirectional excitation and tunneling of SPPs and Kerker conditions. Finally, a conclusion is given in Section 4.

## 2. Materials and Methods

Figure 1a schematically shows the structural unit array of the proposed dielectric–metal metasurface, which consists of  $\text{Al}_2\text{O}_3$  dielectric disks and a thin layer of gold (Au) film on a  $\text{SiO}_2$  substrate. Figure 1b is for one structural unit. The radius of  $\text{Al}_2\text{O}_3$  disk is  $r = 200$  nm and the thicknesses of the Au layer and  $\text{Al}_2\text{O}_3$  disk are  $t_1 = 20$  nm and  $t_2 = 200$  nm, respectively; structural units are periodically arranged with period  $p_x = p_y = 700$  nm. Compared with previous AT devices based on metal–insulator–metal (M–I–M) [22] or metal–metal–metal (M–M–M) subwavelength grating [23], our design can also be viewed as a kind of meta-grating with a relatively simple and easy-to-fabricate structure that can be easily integrated with other optoelectronic devices.

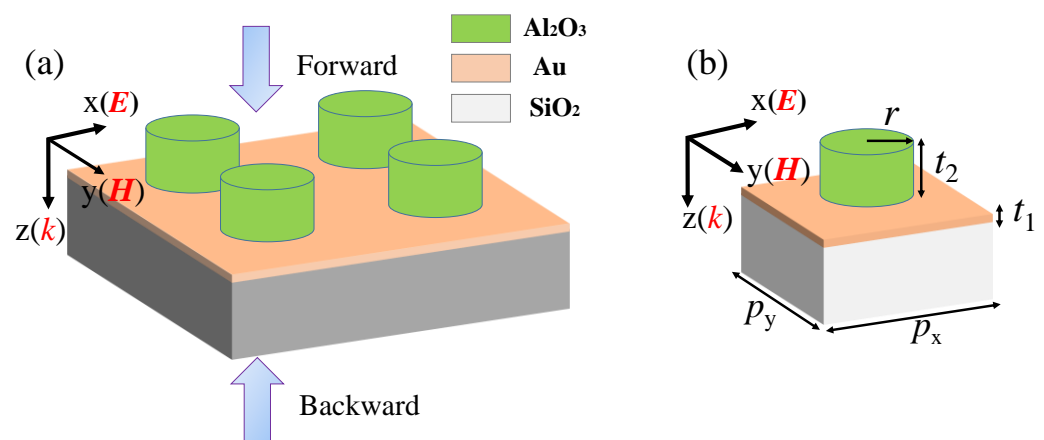


**Figure 1.** Schematic diagrams of the proposed dielectric–metal metasurface. (a) Perspective view of the structural unit arrays of the dielectric–metal metasurface. (b) The optimized geometrical parameters of one unit:  $p_x = p_y = 700$  nm,  $t_1 = 20$  nm,  $t_2 = 200$  nm,  $r = 200$  nm.

In addition, it can be observed that the proposed device has rotational symmetry, meaning it can work under both x- and y-linearly polarized light as well as circularly polarized light. Next, for simplicity, we will just discuss the case of x-polarized incident light.

The operation mechanism of the AT device mainly involves unidirectional SPPs excitation and Kerker conditions. Therefore, we introduce these two aspects below.

### (1) Unidirectional excitation of SPPs

To begin, we explain how unidirectional SPP excitation is produced. When x-polarized incident light illuminates the device in the forward direction (i.e., along the positive z-axis), the light first impinges on the periodically arranged dielectric disks which provide the required wave vector for efficient excitation of surface plasmon polaritons (SPPs), and thus, help electromagnetic energy tunnel through the Au film. By contrast, in the case of backward illumination, the light first hits the Au film. Lacking a periodic structure to

provide an extra wave vector to excite SPPs, the device obtains low backward transmittance, and most of the electromagnetic energy is reflected.

## (2) Kerker conditions

Kerker conditions were first proposed by M. Kerker et al. [34] to study electromagnetic scattering by magnetic spheres with zero backward or zero forward scattering arising from the interference between electric and magnetic dipole modes. A direct conclusion is that when electric dipole (ED) and magnetic dipole (MD) resonances oscillate in-phase with equal magnitudes, the scattered fields are mainly in the direction of the incoming wave with zero-backward radiated power, which is named as the first Kerker condition. Correspondingly, when the two dipoles are of equal magnitude but oscillate out of phase, they may lead to zero forward radiation, which is named as the second Kerker condition. To date, this theory has been expanded to study directional scattering from non-spherical nanostructures containing electric and magnetic multipole resonant modes [35,36].

On the other hand, as is well known, a dielectric nanostructure, such as a nanosphere or a nanodisk, can simultaneously support electric and magnetic responses [37–39]. Therefore, the Al<sub>2</sub>O<sub>3</sub> dielectric disk of a suitable thickness also inherently possesses a strong electric and magnetic dipole or multipolar moments, and the overlap between the ED and MD resonances can greatly enhance forward transmittance at the operation wavelength if we carefully design the metasurface by deliberately employing Kerker conditions. Next, we discuss how Kerker conditions work in our AT device.

When an x-polarized wave normally illuminates the metasurface along the positive z-axis (i.e., the forward propagation direction), the light first hits the dielectric disk array and excites an electric dipole  $p_x$  along the x-axis within each disk. Different from a plasmonic structure, which needs a special profile to excite a circular current to support an equivalent magnetic dipole response, the dielectric disk itself can simultaneously support electric dipole and magnetic dipole responses. Therefore, a magnetic dipole moment  $m_y$  along the y-axis is induced inside the Al<sub>2</sub>O<sub>3</sub> dielectric disk. The normalized forward/backward (i.e., along the positive or negative z-axis) scattering cross-section of the structure unit can be expressed as [40]:

$$Q = \frac{k^4}{4\pi\epsilon^2 A |E_{\text{inc}}|^2} \left| p_x \pm \frac{\sqrt{\epsilon_r} m_y}{c} \right|^2, \quad (1)$$

where  $k$  is the wavenumber in a background material with electric permittivity  $\epsilon = \epsilon_0\epsilon_r$ ,  $c$  is the speed of light in free space, and  $|E_{\text{inc}}|$  is the electric-field amplitude of the incident wave.  $A$  is the geometrical cross-section, and the symbols ‘ $\pm$ ’ represent forward and backward scattering cross sections, respectively.

According to Equation (1), zero backward scattering occurs at some wavelengths when the first Kerker condition is met, which is expressed as:

$$p_x - \frac{\sqrt{\epsilon_r} m_y}{c} = 0, \quad (2)$$

In this case, the scattered field is mainly in the direction of the incoming wave, leading to a zero reflection, and a high transmittance is achieved if optical absorption is also low.

Similarly, zero forward scattering takes place at some wavelengths when the second Kerker condition is fulfilled, which is written as:

$$p_x + \frac{\sqrt{\epsilon_r} m_y}{c} = 0, \quad (3)$$

In this case, the scattered field mainly propagates opposite to the direction of the incoming wave, leading to a zero transmission.

At other wavelengths, if neither the first Kerker condition nor the second Kerker condition is met, then the light will be partly transmitted and partly reflected.

### 3. Results and Discussion

To verify the AT behavior of the proposed dielectric–metal metasurface, we carry out full three-dimensional (3D) finite-difference time-domain (FDTD) simulations by employing the FDTD solver from Lumerical, Inc. to simulate its electromagnetic response and scattering characteristics. Periodic boundary conditions are applied in the  $x$ - and  $y$ -directions, and a perfectly matched layer condition is applied in the  $z$ -direction. The substrate is silica ( $\text{SiO}_2$ ), the dielectric disk is  $\text{Al}_2\text{O}_3$ , and their permittivity values are inferred from Palik refractive index database values [21]. The thin metal layer is gold, and its dielectric constants are taken from Johnson and Christy data, which can also be obtained in the material database from the simulation software. Mesh refinement is used for both the thin metallic film and  $\text{Al}_2\text{O}_3$ ; the mesh sizes in the  $z$ -direction are set as  $dz = 2$  nm and  $dz = 10$  nm, respectively, while the mesh size in the  $x$ - and  $y$ -directions are both set as  $dx = dy = 10$  nm.

#### 3.1. High-Performance Asymmetric Transmission

The simulated transmittance spectra under forward (green solid line) and backward (red dashed line) illumination are shown in Figure 2a. It can be clearly seen that the asymmetric transmission region exists at a cut-off wavelength (i.e.,  $\lambda_A$ ) corresponding to the Wood–Rayleigh anomaly wavelength given by  $\lambda = np$  [41], where  $n$  is the refractive index of the substrate and  $p$  is the structural period. In our case,  $n$  and  $p$  are 1.45 and 700 nm, respectively. Because  $\lambda = np = 1015$  nm, it coincides well with the simulation result  $\lambda_A = 1017$  nm. It should be noted that the cut-off wavelength divides the wavelength domain into a diffraction region ( $\lambda < \lambda_A$ ) and a non-diffraction region ( $\lambda > \lambda_A$ ). Furthermore, the asymmetric transmission phenomenon occurs in the diffraction region [41,42].

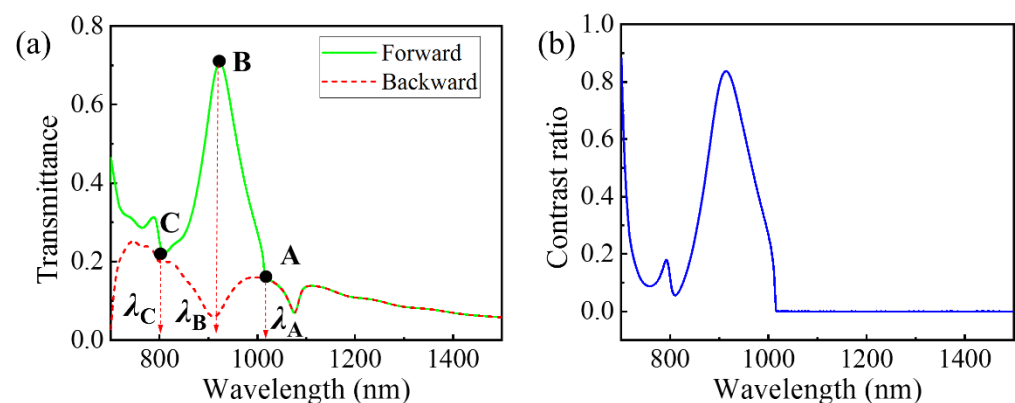


**Figure 2.** (a) Forward and backward transmittance spectra of the metasurface. (b) Contrast ratio versus wavelength. The marked wavelengths are  $\lambda_A = 1017$  nm at point A,  $\lambda_B = 922$  nm at point B, and  $\lambda_C = 800$  nm at point C.

Moreover, a very interesting phenomenon can be clearly seen in Figure 2a, where the forward transmission peak and backward transmission dip occur at the same wavelength  $\lambda_B = 922$  nm. When propagating in the forward direction, the optical wave at this wavelength is a transmittance peak, with a transmittance of 0.70. However, when this wave backwardly illuminates the metasurface, a transmittance dip is observed, with a very low transmittance of 0.07. This is quite different from previously reported AT works. To the best of our knowledge, such a phenomenon has not been reported yet.

A good asymmetric transmission device requires not only a higher forward transmittance but also a larger contrast ratio and wide operation bandwidth. A contrast ratio is used to evaluate the degree of asymmetric transmission, which is defined as:

$$\text{contrast ratio} = \frac{|T_f - T_b|}{T_f + T_b}, \quad (4)$$

where  $T_f$  and  $T_b$  are the forward and backward transmittances, respectively.

As shown in Figure 2b, the contrast ratio reaches 0.82 at  $\lambda_B = 922$  nm, and the full width at half maximum (FWHM) is 100 nm, which means the proposed dielectric–metal metasurface has a large wide operation bandwidth. The reason for the high contrast ratio and big bandwidth mainly lies in the fact that the forward transmission peak and backward transmission dip occur at the same wavelength.

In what follows, we will further reveal how the device achieves high-performance asymmetric transmission.

### 3.2. Mechanism Analyses on Asymmetric Transmission

To demonstrate how the unidirectional excitation of SPPs works in our device, Figure 3 shows the corresponding  $E_z$  electric-field distributions at  $\lambda_B = 922$  nm, where the white dotted lines mark the locations of the dielectric disks and the black dotted line marks that of the metal layer. As can be clearly seen in Figure 3a, under forward illumination, SPPs with wavelength  $\lambda_{SPP} = 708$  nm are excited in the dielectric–metal interface, then tunnel through the Au film and, finally, enter the SiO<sub>2</sub> substrate, meaning a high forward transmittance is obtained. In contrast, for backward incident light at  $\lambda_B = 922$  nm, the electric field intensity is too weak to see obvious excitation of SPPs, as shown in Figure 3b. This result occurs when the incident direction is reversed because the light first hits the Au film. On the one hand, there are no periodically arranged resonators to provide the extra wave vector to efficiently excite SPPs. On the other hand, the Au film in this case works as a high-efficiency reflector. As a result, most of the electromagnetic energy is reflected by the Au film.

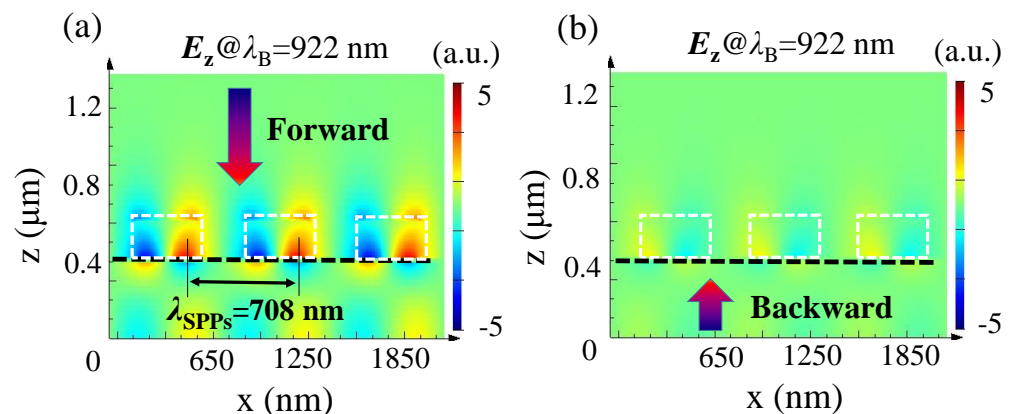


**Figure 3.** Electric-field  $E_z$  distributions along the  $x$ - $z$  plane at  $\lambda_B = 922$  nm under forward (a) and backward (b) illumination.

However, the appearance of SPPs does not guarantee that the corresponding transmittance will be very high. Next, we will further investigate how the device can achieve a forward transmission peak and backward transmission dip at the same wavelength of 922 nm.

#### 3.2.1. Role of Kerker Conditions in the Realization of the Forward Transmission Peak

Above, we have offered a preliminary analysis on the origin of the asymmetric transmission; now, we further investigate how the forward transmission peak is achieved at  $\lambda_B = 922$  nm. As mentioned earlier, Kerker conditions are usually adopted to explain electromagnetic scattering characteristics in many metasurface systems, such as perfect transmission [36,43], and asymmetric transmission (AT) [21,22].

Here, in order to investigate how Kerker conditions are satisfied in our AT device, we choose two specific wavelengths for comparative analysis: one is  $\lambda_B = 922$  nm, at which forward transmittance has a maximal value of 0.70, and the other is  $\lambda_C = 800$  nm, at which forward transmittance reaches a minimal value of 0.21. Figure 4(a1,a2) and

Figure 4(b1,b2) plot their electromagnetic field distribution profiles in the x–y plane under forward incidence.

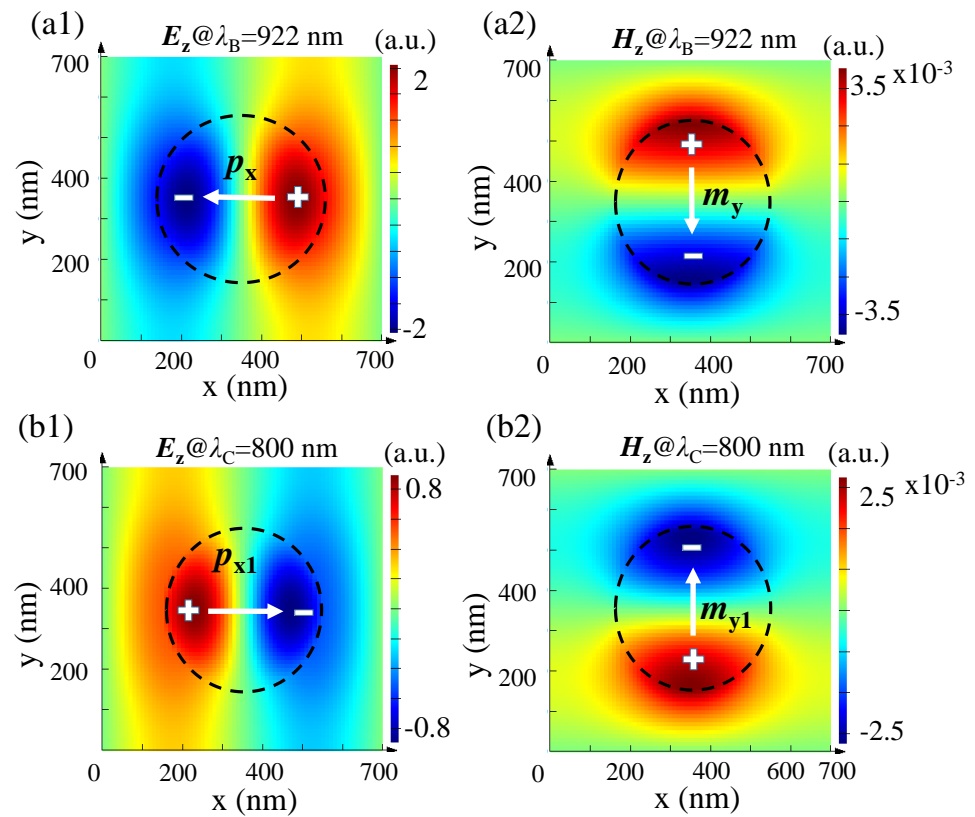


**Figure 4.** Electromagnetic field distribution in the x–y plane for forward incidence light. (a1) Electric dipole and (a2) magnetic dipole at  $\lambda_B = 922$  nm. (b1) Electric dipole and (b2) magnetic dipole at  $\lambda_C = 800$  nm. The black dotted line marks the outline of the  $\text{Al}_2\text{O}_3$  disk. The white arrow stands for the direction of the electric or magnetic dipole.

At  $\lambda_B = 922$  nm, when the metasurface is forwardly illuminated by x-polarized light, a strong  $E_z$  field is excited in the dielectric disk (marked by the black dashed line in Figure 4(a1)), and the stimulated positive (marked as '+') and negative (marked as '-') charges are formed, which give rise to an electric-dipole moment  $p_x$  oscillating along the negative x-axis (the white arrow stands for the direction of the electric dipole). Meanwhile, as shown in Figure 4(a2), the dielectric disk also supports a magnetic dipolar  $m_y$  along the negative y-axis.  $p_x$  and  $m_y$  are both along the negative directions, signifying that the radiated fields from  $p_x$  and  $m_y$  oscillations are nearly in phase; hence, their overlap causes strong suppression in reflection, which implies that the first Kerker condition is satisfied and zero backward scattering occurs. As a consequence, a forward transmittance peak, with a transmittance of 0.70, appears at  $\lambda_B = 922$  nm.

At  $\lambda_C = 800$  nm, Figure 4(b1) shows electric dipole  $p_{x1}$  is along the positive direction of the x-axis, and the induced magnetic-dipole moment  $m_{y1}$  is along the positive y-axis, as shown in Figure 4(b2). Therefore, the radiated fields from  $p_{x1}$  and  $m_{y1}$  oscillations are also nearly in phase. However, by comparing the electric- and magnetic-dipole distributions at  $\lambda_C$  (see Figure 4(b1,b2)) with those at  $\lambda_B$  (see Figure 4(a1,a2)), one can see that the amplitude of  $p_{x1}$  at  $\lambda_C = 800$  nm is much lower than that of  $p_x$  at  $\lambda_B = 922$  nm, and the amplitude of  $m_{y1}$  at  $\lambda_C = 800$  nm is close to that of  $m_y$  at  $\lambda_B = 922$  nm. Nevertheless, the large difference in amplitudes of  $p_{x1}$  and  $m_{y1}$  infers that the interaction between them cannot lead to a good interference to obtain high forward transmittance at  $\lambda_C = 800$  nm. As a consequence, the forward transmittance at  $\lambda_C = 800$  nm has a value of only 0.21.

### 3.2.2. Realization of the Low Backward Transmittance Dip

After analyzing the origin of the forward transmittance peak at  $\lambda_B = 922$  nm, we now continue to investigate the origin of the low backward transmittance dip at the same wavelength.

In the discussion of Figure 3b, we already explained that the lack of efficient excitation of SPPs and the back reflection by the Au film contribute to the low backward transmittance. However, this cannot explain why a transmittance dip with a near-zero transmittance appears at  $\lambda_B$ .

We know that geometrical parameters of a device determine its electromagnetic (EM) response, thus affecting its scattering characteristics when it interacts with electromagnetic waves [44,45]. As a kind of scattering, the characteristic transmittance curve is also directly affected by different electromagnetic responses. In this regard, it is common to study their resonant properties in terms of electric and magnetic multipoles, which can be derived from the Taylor expansion of their EM fields and potentials [46]. Here, we only consider electric dipole (ED), magnetic dipole (MD), electric quadrupole (EQ), magnetic quadrupole (MQ) and toroidal dipole (TD), because higher-order electric and magnetic resonance modes cannot be excited. In a Cartesian coordinate system, the multipole decomposition can be, respectively, written as [47]:

$$\mathbf{P} = \frac{1}{i\omega} \int \mathbf{j} d^3r, \quad (5)$$

$$\mathbf{M} = \frac{1}{2c} \int (\mathbf{r} \times \mathbf{j}) d^3r, \quad (6)$$

$$QE_{\alpha\beta} = \frac{1}{i\omega} \int \left[ (r_\alpha j_\beta + r_\beta j_\alpha) - \frac{2}{3} (\mathbf{r} \cdot \mathbf{j}) \right] d^3r, \quad (7)$$

$$QM_{\alpha\beta} = \frac{1}{3c} \int \left[ (\mathbf{r} \times \mathbf{j})_\alpha j_\beta + (\mathbf{r} \times \mathbf{j})_\beta j_\alpha \right] d^3r, \quad (8)$$

$$\mathbf{T} = \frac{1}{10c} \int \left[ (\mathbf{r} \cdot \mathbf{j}) \mathbf{r} - 2r^2 \mathbf{j} \right] d^3r. \quad (9)$$

where  $c$  is the speed of light,  $\mathbf{j}$  is current density,  $\omega$  is the angular frequency of the electromagnetic wave and  $\mathbf{r}$  is the position vector from the origin to point  $(x, y, z)$  in a Cartesian coordinate system ( $\alpha, \beta = x, y, z$ ).  $\mathbf{P}$ ,  $\mathbf{M}$ ,  $QE_{\alpha\beta}$ ,  $QM_{\alpha\beta}$ , and  $\mathbf{T}$  are the electric dipole (ED) moment, magnetic dipole (MD) moment, electric quadrupole (EQ) moment, magnetic quadrupole (MQ) moment and toroidal dipole (TD) moment, respectively.

The corresponding radiated light powers are calculated by [47]:

$$I_P = \frac{2\omega^4}{3c^3} |\mathbf{P}|^2, \quad (10)$$

$$I_M = \frac{2\omega^4}{3c^3} |\mathbf{M}|^2 \quad (11)$$

$$I_T = \frac{2\omega^6}{3c^5} |\mathbf{T}|^2, \quad (12)$$

$$I_{QE} = \frac{\omega^6}{5c^5} \sum |QE_{\alpha\beta}|^2, \quad (13)$$

$$I_{QM} = \frac{\omega^6}{20c^5} \sum |QM_{\alpha\beta}|^2. \quad (14)$$

According to Equations (10)–(14), we calculate electromagnetic multipolar dipoles under backward illumination and present the results in Figure 5a. As shown, near  $\lambda_B = 922$  nm, the toroidal dipole (TD) has the strongest scattering power while the electric quadrupole (EQ) ranks second; other electromagnetic multipoles account for a small proportion, especially the electric dipole (ED) and the magnetic dipole (MD), which are

strongly suppressed. These results demonstrate that the resonance at  $\lambda_B = 922$  nm is dominated by the toroidal dipole moment.

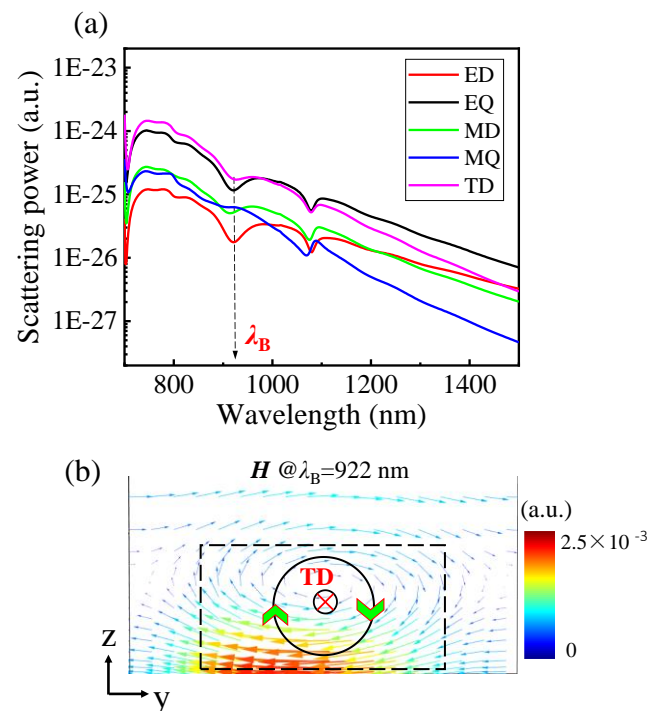


**Figure 5.** (a) Scattering spectra for ED, MD, EQ, MQ, and TD modes under backward illumination. (b) Cross-sectional vectorial ( $y$ - $z$  plane) for the magnetic-field ( $H$ -field) maps for the excitation of toroidal dipole (TD). The black dashed line marks the outline of  $\text{Al}_2\text{O}_3$  disk, while the black circular lines along the circumference indicate toroidal moment. The green arrow marks the circular magnetic field direction, and the direction of TD is shown by the symbol  $\otimes$ .

As we know, the toroidal dipole (TD), as an independent family of elementary electromagnetic source, corresponds to electric currents flowing on the surface of a torus. However, toroidal dipole response in electrodynamics is often masked by the more dominant electric and magnetic multipoles at a similar frequency. Recently, due to its nonradiating feature, toroidal dipole has attracted increasing attention in metasurface research, and it provides many interesting phenomena with enhanced light-matter interactions and applications in spasers [48], ultrasensitive biosensing [49] and nonlinear effects [50]. However, the application of toroidal dipole in asymmetric transmission has not been reported yet. As can be clearly seen in Figure 5a, the scattering of the toroidal dipole (TD) corresponds to a dip at  $\lambda_B$ , and other electromagnetic poles, except for the magnetic quadrupole (MQ), also exhibit a resonance dip at this wavelength. These dips demonstrate the appearance of a low backward transmittance dip at  $\lambda_B = 922$  nm.

Based on the above discussion, we believe that the lack of efficient excitation of SPPs, the back reflection by the Au film and the dominant toroidal dipole response together contribute to the appearance of a backward transmittance dip at  $\lambda_B = 922$  nm.

To further verify the existence of TD, the cross-sectional ( $y$ - $z$  plane) magnetic-field ( $H$ -field) at  $\lambda_B = 922$  nm is plotted in Figure 5b, in which the black dashed line shows the position of the  $\text{Al}_2\text{O}_3$  dielectric disk. As shown, the poloidal magnetic field spins in a clockwise path in the  $\text{Al}_2\text{O}_3$  dielectric disk, which can explain the existence of the toroidal dipole (TD), represented by the black circle line in Figure 5b, while the green arrow marks the circular magnetic field direction.

Furthermore, from Figure 5b, one can see that the circulating magnetic fields are mainly located inside the dielectric disk; hence, changing the thickness of the dielectric disk will have a significant impact on the transmittance response.



### 3.2.3. Effect of the Thickness of the Dielectric Disk and Au Layer on Asymmetric Transmission

Besides the disk thickness mentioned above, which has a significant effect on transmission spectrum, the metal layer's thickness is also crucial because it plays a key role in the tunneling of SPPs and impacts transmittance spectra. Therefore, it is necessary to choose suitable thicknesses for the Au film and dielectric disk.

Firstly, as shown in Figure 6a, when the thickness of the gold (Au) layer,  $t_1$ , increases from 20 nm to 40 nm by a step of 10 nm (while other geometric parameters remain unchanged), both the forward (F) and backward (B) transmittance spectra tend to decrease. Obviously, in the case of forward incidence, it is more difficult for the SPPs to tunnel through a thicker Au layer, whereas in the case of backward incidence, a thicker Au layer reflects more light. As a result, both forward and backward transmission decreases with the increase in Au thickness.

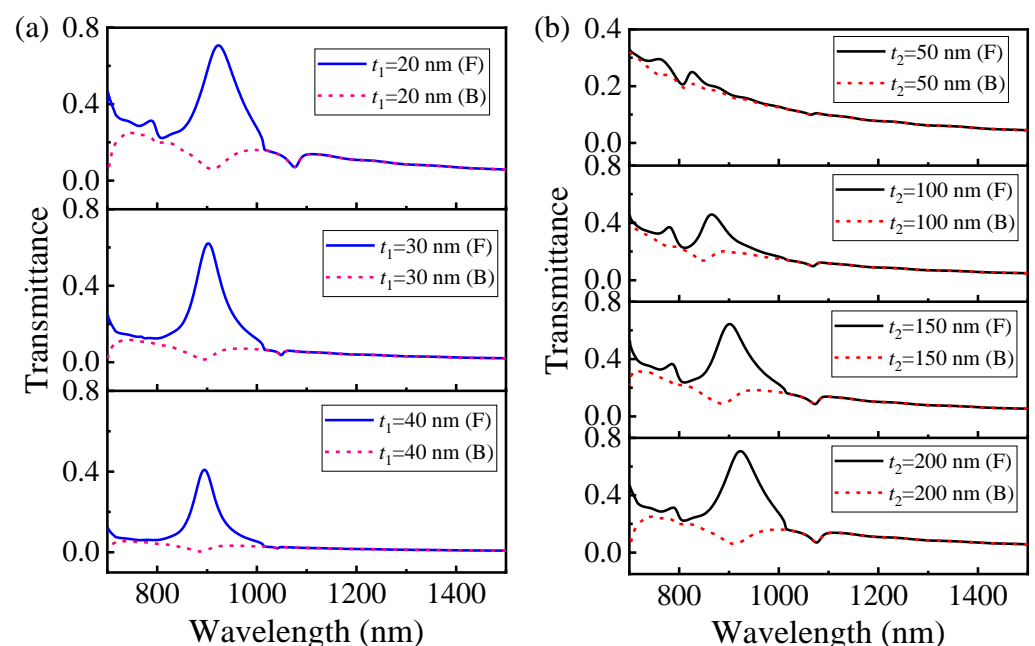


**Figure 6.** Forward (F) and backward (B) transmittance spectra for different geometric parameters. (a) Au layer thickness  $t_1$ ; (b) dielectric disk thickness  $t_2$ .

Secondly, as shown in Figure 6b, when the thickness of the dielectric disk  $t_2$  is 50 nm, the maximal forward transmittance is only 0.3. With the increase in  $t_2$  (while other geometric parameters remain unchanged), the peak value of forward transmittance increases gradually. Most notably, when  $t_2$  increases to 200 nm, the maximal forward transmittance is close to 0.70 at 922 nm. This can be understood as follows: when  $t_2$  is small, it is hard to excite the annular displacement current inside the dielectric disk; thus, an effective magnetic response is unable to form [51,52], which affects the interference effect between electromagnetic multipolar moments. Therefore, in this paper, we choose  $t_2 = 200$  nm as the optimization thickness for the dielectric disks.

In addition, under backward illumination, when  $t_2$  increases from 50 nm to 200 nm, the transmission dip gradually redshifts, and its corresponding transmittance also decreases. This is especially noticeable when  $t_2$  increases to 200 nm, for its value is only 0.07 at  $\lambda_B = 922$  nm. This is because the toroidal dipole response gradually rises to the dominant position; thus, it further suppresses transmission and, finally, leads to a low transmittance dip at  $\lambda_B = 922$  nm.

#### 4. Conclusions

In summary, we propose and numerically demonstrate a dielectric–metal metasurface that can work as a high-performance asymmetric transmission (AT) device in the near-infrared region. The simulation results show that it can support a forward transmittance peak (with a transmittance of 0.70) and a backward transmittance dip (with a transmittance of 0.07) at wavelength 922 nm. The occurrence of a forward transmission peak and backward transmission dip at the same wavelength notably enhances the operation bandwidth and the contrast ratio between the forward and backward transmittances, and this feature is quite different from previously reported devices. The physical mechanism behind this extraordinary phenomenon is investigated with respect to the unidirectional excitation of surface plasmon polaritons (SPPs), Kerker conditions and the electromagnetic multipole decomposition method. To be specific, when the light is forwardly incident on the proposed dielectric–metal metasurface, the dielectric disk and the metal film excite SPPs; meanwhile, the electric and magnetic responses within the dielectric disk satisfy the first Kerker condition so that the electromagnetic energy can tunnel through the metal layer with the assistance of SPPs, realizing a transmittance peak at 922 nm. However, when the incident direction is reversed, the light cannot pass the device due to the lack of effective SPPs excitation, resulting in most electromagnetic energy being reflected by the metal layer. At the same time, the nonradiating toroidal dipole dominates in the far-field scattering powers, and it further promotes the formation of a transmittance dip at 922 nm.

In view of its simple structure and excellent performance, we believe that the proposed metasurface shows extensive versatility for potential applications including, but not limited to, noise control, one-side detection, optical beam splitters and other photonic devices.

**Author Contributions:** Conceptualization, W.L. and L.H.; software, W.L.; validation, C.X., J.D. and Y.L.; formal analysis, W.L., L.H., W.H.; writing—original draft preparation, W.L.; writing—review and editing, L.H., W.H.; funding acquisition, L.H. All authors have read and agreed to the published version of the manuscript.

**Funding:** This research was funded by the National Science Foundation of China (61675074).

**Institutional Review Board Statement:** Not applicable.

**Informed Consent Statement:** Not applicable.

**Data Availability Statement:** Data are contained within the article.

**Acknowledgments:** We thank the National Natural Science Foundation of China.

**Conflicts of Interest:** The authors declare no conflict of interest.

#### References

1. Jalas, D.; Petrov, A.; Eich, M.; Freude, W.; Fan, S.; Yu, Z.; Baets, R.; Popović, M.; Melloni, A.; Joannopoulos, J.D.; et al. What is-and what is not-an optical isolator. *Nat. Photonics* **2013**, *7*, 579–582. [[CrossRef](#)]
2. Liu, N.; Zhao, J.; Du, L.; Niu, C.; Sun, C.; Kong, X.; Wang, Z.; Li, X. Giant nonreciprocal transmission in low-biased gyrotropic metasurfaces. *Opt. Lett.* **2020**, *45*, 5917. [[CrossRef](#)]
3. Fan, L.; Wang, J.; Varghese, L.T.; Shen, H.; Niu, B.; Xuan, Y.; Weiner, A.M.; Qi, M. An all-silicon passive optical diode. *Science* **2012**, *335*, 447–450. [[CrossRef](#)] [[PubMed](#)]
4. Zhao, N.-S.; Zhou, H.; Guo, Q.; Hu, W.; Yang, X.-B.; Lan, S.; Lin, X.-S. Design of highly efficient optical diodes based on the dynamics of nonlinear photonic crystal molecules. *J. Opt. Soc. Am. B* **2006**, *23*, 2434. [[CrossRef](#)]
5. Sounas, D.L.; Alù, A. Non-reciprocal photonics based on time modulation. *Nat. Photonics* **2017**, *11*, 774–783. [[CrossRef](#)]
6. Chin, J.Y.; Steinle, T.; Wehlius, T.; Dregely, D.; Weiss, T.; Belotelov, V.I.; Stritzker, B.; Giessen, H. Nonreciprocal plasmonics enables giant enhancement of thin-film Faraday rotation. *Nat. Commun.* **2013**, *4*, 1596–1599. [[CrossRef](#)] [[PubMed](#)]
7. Zhu, Z.H.; Liu, K.; Xu, W.; Luo, Z.; Guo, C.C.; Yang, B.; Ma, T.; Yuan, X.D.; Ye, W.M. One-way transmission of linearly polarized light in plasmonic subwavelength metallic grating cascaded with dielectric grating. *Opt. Lett.* **2012**, *37*, 4008. [[CrossRef](#)]
8. Cakmakyapan, S.; Caglayan, H.; Serebryannikov, A.E.; Ozbay, E. Experimental validation of strong directional selectivity in nonsymmetric metallic gratings with a subwavelength slit. *Appl. Phys. Lett.* **2011**, *98*, 7–10. [[CrossRef](#)]
9. Bi, L.; Hu, J.; Jiang, P.; Kim, D.H.; Dionne, G.F.; Kimerling, L.C.; Ross, C.A. On-chip optical isolation in monolithically integrated non-reciprocal optical resonators. *Nat. Photonics* **2011**, *5*, 758–762. [[CrossRef](#)]

10. Bi, Y.; Huang, L.; Li, X.; Wang, Y. Magnetically controllable metasurface and its application. *Front. Optoelectron.* **2021**, *14*, 154–169. [[CrossRef](#)]
11. Lepri, S.; Casati, G. Asymmetric wave propagation in nonlinear systems. *Phys. Rev. Lett.* **2011**, *106*, 164101. [[CrossRef](#)] [[PubMed](#)]
12. Ji, R.; Jin, C.; Song, K.; Wang, S.W.; Zhao, X. Design of multifunctional janus metasurface based on subwavelength grating. *Nanomaterials* **2021**, *11*, 1034. [[CrossRef](#)]
13. Jing, L.; Lin, X.; Wang, Z.; Kammer, I.; Hu, H.; Li, E.; Liu, Y.; Chen, M.; Zhang, B.; Chen, H. Polarization Shaping of Free-Electron Radiation by Gradient Bianisotropic Metasurfaces. *Laser Photonics Rev.* **2021**, *15*, 2000426. [[CrossRef](#)]
14. Liu, S.; Dong, J.; Si, J.; Yang, W.; Yu, X.; Zhang, J.; Deng, X. Bidirectional electromagnetically induced transparency based on coupling of magnetic dipole modes in amorphous silicon metasurface. *Nanomaterials* **2021**, *11*, 1550. [[CrossRef](#)]
15. Shields, J.; de Galarreta, C.R.; Bertolotti, J.; Wright, C.D. Enhanced performance and diffusion robustness of phase-change metasurfaces via a hybrid dielectric/plasmonic approach. *Nanomaterials* **2021**, *11*, 525. [[CrossRef](#)] [[PubMed](#)]
16. Zhang, J.; Yu, X.; Dong, J.; Yang, W.; Liu, S.; Shen, C.; Duan, J.; Deng, X. A plasmonic infrared multiple-channel filter based on gold composite nanocavities metasurface. *Nanomaterials* **2021**, *11*, 1824. [[CrossRef](#)]
17. Zhen, Z.; Qian, C.; Jia, Y.; Fan, Z.; Hao, R.; Cai, T.; Zheng, B.; Chen, H.; Li, E. Realizing transmitted metasurface cloak by a tandem neural network. *Photonics Res.* **2021**, *9*, B229. [[CrossRef](#)]
18. Fedotov, V.A.; Mladyonov, P.L.; Prosvirnin, S.L.; Rogacheva, A.V.; Chen, Y.; Zheludev, N.I. Asymmetric propagation of electromagnetic waves through a planar chiral structure. *Phys. Rev. Lett.* **2006**, *97*, 167401. [[CrossRef](#)]
19. Cakmak, A.O.; Colak, E.; Serebryannikov, A.E.; Ozbay, E. Unidirectional transmission in photonic-crystal gratings at beam-type illumination. *Opt. Express* **2010**, *18*, 22283. [[CrossRef](#)] [[PubMed](#)]
20. Wang, Z.; Chong, Y.D.; Joannopoulos, J.D.; Soljačić, M. Reflection-free one-way edge modes in a gyromagnetic photonic crystal. *Phys. Rev. Lett.* **2008**, *100*, 772–775. [[CrossRef](#)]
21. Ling, Y.; Huang, L.; Liu, T.; Sun, Y.; Luan, J.; Hong, W.; Yuan, G. Asymmetric electromagnetic wave transmitter based on one-way excitation of surface plasmon polaritons in gradient metasurface. *Opt. Express* **2017**, *25*, 13648–13658. [[CrossRef](#)] [[PubMed](#)]
22. Li, S.; Huang, L.R.; Ling, Y.H.; Liu, W.B.; Ba, C.F.; Li, H.H. High-performance asymmetric optical transmission based on coupled complementary subwavelength gratings. *Sci. Rep.* **2019**, *9*, 17117. [[CrossRef](#)] [[PubMed](#)]
23. Ba, C.; Huang, L.; Liu, W.; Li, S.; Ling, Y.; Li, H. Narrow-band and high-contrast asymmetric transmission based on metal-metal asymmetric gratings. *Opt. Express* **2019**, *27*, 25107. [[CrossRef](#)] [[PubMed](#)]
24. Khalichi, B.; Ghobadi, A.; Osgouei, A.K.; Ozbay, E. Diode like high-contrast asymmetric transmission of linearly polarized waves based on plasmon-tunneling effect coupling to electromagnetic radiation modes. *J. Phys. D Appl. Phys.* **2021**, *54*, 365102. [[CrossRef](#)]
25. Li, Z.; Mutlu, M.; Ozbay, E. Highly asymmetric transmission of linearly polarized waves realized with a multilayered structure including chiral metamaterials. *J. Phys. D Appl. Phys.* **2014**, *47*, 075107. [[CrossRef](#)]
26. Xiao, Z.; Liu, D.; Ma, X.; Wang, Z. Multi-band transmissions of chiral metamaterials based on Fabry-Perot like resonators. *Opt. Express* **2015**, *23*, 7053. [[CrossRef](#)]
27. Li, X.; Feng, R.; Ding, W. Extremely high contrast asymmetric transmission with linear tunability in chiral metamaterials. *J. Phys. D. Appl. Phys.* **2018**, *51*, 145304. [[CrossRef](#)]
28. Liu, W.; Wu, W.; Huang, L.; Ling, Y.; Ba, C.; Li, S.; Chun, Z.; Li, H. Dual-band asymmetric optical transmission of both linearly and circularly polarized waves using bilayer coupled complementary chiral metasurface. *Opt. Express* **2019**, *27*, 33399. [[CrossRef](#)]
29. Dong, X.; Luo, X.; Zhou, Y.; Lu, Y.; Hu, F.; Xu, X.; Li, G. Switchable broadband and wide-angular terahertz asymmetric transmission based on a hybrid metal-VO<sub>2</sub> metasurface. *Opt. Express* **2020**, *28*, 30675. [[CrossRef](#)]
30. Fu, T.; Liu, F.; An, Y.; Li, Q.; Xiao, G.; Sun, T.; Li, H. Narrow-band asymmetric transmission based on the dark mode of Fano resonance on symmetric trimeric metasurfaces. *Opt. Express* **2020**, *28*, 30141. [[CrossRef](#)]
31. Kenanakis, G.; Xomalis, A.; Selimis, A.; Vamvakaki, M.; Farsari, M.; Kafesaki, M.; Soukoulis, C.M.; Economou, E.N. Three-dimensional infrared metamaterial with asymmetric transmission. *ACS Photonics* **2015**, *2*, 287–294. [[CrossRef](#)]
32. Parappurath, N.; Alpeggiani, F.; Kuipers, L.; Verhagen, E. The Origin and Limit of Asymmetric Transmission in Chiral Resonators. *ACS Photonics* **2017**, *4*, 884–890. [[CrossRef](#)]
33. Mutlu, M.; Akosman, A.E.; Serebryannikov, A.E.; Ozbay, E. Diodelike asymmetric transmission of linearly polarized waves using magnetoelectric coupling and electromagnetic wave tunneling. *Phys. Rev. Lett.* **2012**, *108*, 213905. [[CrossRef](#)]
34. Kerker, M.; Wang, D.S.; Giles, C.L. Electromagnetic Scattering by Magnetic Spheres. *J. Opt. Soc. Am.* **1983**, *73*, 765–767. [[CrossRef](#)]
35. Fan, K.; Shadrivov, I.V.; Miroshnichenko, A.E.; Padilla, W.J. Infrared all-dielectric Kerker metasurfaces. *Opt. Express* **2021**, *29*, 10518. [[CrossRef](#)] [[PubMed](#)]
36. Liu, W.; Kivshar, Y.S. Generalized Kerker effects in nanophotonics and meta-optics. *arXiv* **2017**, *26*, 274–284. [[CrossRef](#)]
37. Ding, J.; Huang, L.; Liu, W.; Ling, Y.; Wu, W.; Li, H. Mechanism and performance analyses of optical beam splitters using all-dielectric oligomer-based metasurfaces. *Opt. Express* **2020**, *28*, 32721–32737. [[CrossRef](#)]
38. Wan, L.; Pan, D.; Feng, T.; Liu, W.; Potapov, A.A. A review of dielectric optical metasurfaces for spatial differentiation and edge detection. *Front. Optoelectron.* **2021**, *14*, 187–200. [[CrossRef](#)]
39. Cheng, L.; Alaei, R.; Safari, A.; Karimi, M.; Zhang, L.; Boyd, R.W. Superscattering, Superabsorption, and Nonreciprocity in Nonlinear Antennas. *ACS Photonics* **2021**, *8*, 585–591. [[CrossRef](#)]

40. Alaee, R.; Albooyeh, M.; Yazdi, M.; Komjani, N.; Simovski, C.; Lederer, F.; Rockstuhl, C. Magnetolectric coupling in nonidentical plasmonic nanoparticles: Theory and applications. *Phys. Rev. B Condens. Matter Mater. Phys.* **2015**, *91*, 115119. [[CrossRef](#)]
41. Tang, B.; Li, Z.; Liu, Z.; Callewaert, F.; Aydin, K. Broadband asymmetric light transmission through tapered metallic gratings at visible frequencies. *Sci. Rep.* **2016**, *6*, 39166a. [[CrossRef](#)]
42. Ozer, A.; Kocer, H.; Kurt, H. Broadband and polarization-independent asymmetric transmission of visible light through a three-dimensional trapezoidal metallic metasurface. *J. Opt. Soc. Am. B* **2018**, *35*, 2111. [[CrossRef](#)]
43. Fu, Y.H.; Kuznetsov, A.I.; Miroshnichenko, A.E.; Yu, Y.F.; Luk'yanchuk, B. Directional visible light scattering by silicon nanoparticles. *Nat. Commun.* **2013**, *4*, 1527. [[CrossRef](#)] [[PubMed](#)]
44. Terekhov, P.D.; Babicheva, V.E.; Baryshnikova, K.V.; Shalin, A.S.; Karabchevsky, A.; Evlyukhin, A.B. Multipole analysis of dielectric metasurfaces composed of nonspherical nanoparticles and lattice invisibility effect. *Phys. Rev. B* **2019**, *99*. [[CrossRef](#)]
45. Evlyukhin, A.B.; Chichkov, B.N. Multipole decompositions for directional light scattering. *Phys. Rev. B* **2019**, *100*, 125415. [[CrossRef](#)]
46. Talebi, N.; Guo, S.; Van Aken, P.A. Theory and applications of toroidal moments in electrodynamics: Their emergence, characteristics, and technological relevance. *Nanophotonics* **2018**, *7*, 93–110. [[CrossRef](#)]
47. Savinov, V.; Fedotov, V.A.; Zheludev, N.I. Toroidal dipolar excitation and macroscopic electromagnetic properties of metamaterials. *Phys. Rev. B* **2014**, *89*, 205112. [[CrossRef](#)]
48. Huang, Y.W.; Chen, W.T.; Wu, P.C.; Fedotov, V.A.; Zheludev, N.I.; Tsai, D.P. Toroidal lasing spaser. *Sci. Rep.* **2013**, *3*, 1237. [[CrossRef](#)] [[PubMed](#)]
49. Ahmadvand, A.; Gerislioglu, B.; Pala, N.; Member, S. Large-Modulation-Depth Polarization-Sensitive. *IEEE Photonics Technol. Lett.* **2017**, *29*, 1860–1863. [[CrossRef](#)]
50. Ahmadvand, A.; Semmlinger, M.; Dong, L.; Gerislioglu, B.; Nordlander, P.; Halas, N.J. Toroidal Dipole-Enhanced Third Harmonic Generation of Deep Ultraviolet Light Using Plasmonic Meta-atoms. *Nano Lett.* **2019**, *19*, 605–611. [[CrossRef](#)]
51. Koshelev, K.; Kivshar, Y. Dielectric Resonant Metaphotonics. *ACS Photonics* **2021**, *8*, 102–112. [[CrossRef](#)]
52. Hu, J.; Lawrence, M.; Dionne, J.A. High Quality Factor Dielectric Metasurfaces for Ultraviolet Circular Dichroism Spectroscopy. *ACS Photonics* **2020**, *7*, 36–42. [[CrossRef](#)]